

THE EFFECT OF SHOCK CONTROL BUMPS ON THE TRANSONIC FLUTTER AND BUFFETING CHARACTERISTICS OF A TYPICAL WING SECTION

Jens Nitzsche¹, Jonathan Otte¹, Christoph Kaiser¹, Holger Hennings¹

¹Institute of Aeroelasticity, German Aerospace Center (DLR)
37073 Göttingen, Germany
jens.nitzsche@dlr.de

Keywords: Unsteady aerodynamics, transonic dip, transonic buffet, fluid-mode flutter, flow separation, shock control bumps

Abstract: We investigate the effects of small-scale airfoil geometry modifications, in particular so-called shock control bumps (SCB), on the transonic flutter and buffeting behavior of a classical two-degree-of-freedom model employing linearized stability analysis. The unsteady aerodynamic forces are modelled by solving the discretized RANS equations with respect to small-perturbation mesh deformation input. Special emphasis is put on the coupling of fluid modes and structural modes. SCBs that are designed initially towards purely aerodynamic buffet suppression perform also well in the aeroelastic analysis with respect to fluid-mode flutter. Classical flutter and buffeting are found to be separated by an apparent wall of stability. It is further noted that SCBs can potentially serve to improve the classical flutter behavior in the transonic dip region.

1 INTRODUCTION

The design of future eco-efficient transport aircraft configurations could be increasingly driven by flutter stability and vibration issues due to the expected increase in wing aspect ratio that results from the desire to slash induced drag. These anticipated unsteady fluid-structure interaction problems naturally occur at the high-speed edge of the flight envelope where strong re-compression shocks and flow separation become dominant [1]. In this regime, one of the most interesting phenomena from an aeroelastic point of view is the so-called transonic buffet or *shock buffet*. It is characterized by large-scale, self-sustained shock wave oscillations on the lifting surfaces. It is meanwhile known as a special case of a more general *aerodynamic resonance* behavior inherent to flows involving shock-induced separation, sometimes being termed *pre-buffet flows* [2, 3, 4, 5].

Most of the scientific work on the matter has been concentrating on the identification of the *shock buffet onset*, i.e. the critical flow parameter combination (usually Mach number, angle of attack, Reynolds number), at which the pre-buffet flow undergoes a Hopf bifurcation from a stable steady state to a stable unsteady limit-cycle oscillation. This search for a pure fluid instability has so far usually been carried out with complete neglect of the elasticity of the fluid boundary, i.e. on static geometries. This approach is based on the assumption that the actual structural motion due to the flow instability (termed *buffeting*) – in the sense of a pure structural *response* – results solely from the aerodynamic loads after exceeding the buffet onset. However,

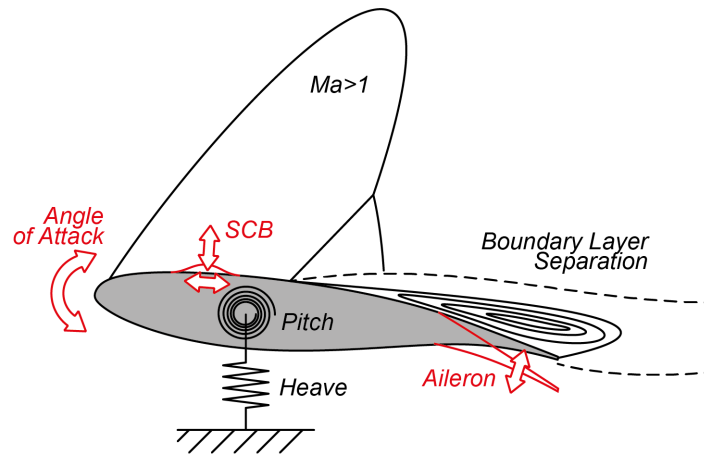


Figure 1: Schematic view of the baseline flow field around the 2-DOF typical-section rectangular wing including the variable steady geometric modifications to be investigated (in red)

recent numerical findings suggest that this assumption may be an oversimplification. Instead, it appears that buffeting, just like flutter, is a coupled stability problem, but with the special feature that the coupling of structural modes characteristic for classical flutter takes place here between a so-called fluid mode and a structural mode (fluid-mode flutter) [6, 5, 7, 8].

In addition to the determination of the buffet onset and with the aim of avoiding potentially detrimental structural vibrations, ways are increasingly being sought to control or completely suppress buffeting through dedicated flow control measures. Analogous to this, there is also an increasing demand for the suppression of classical flutter in order to possibly open up additional degrees of design freedom. In addition to servo-active control measures, so called semi-active approaches are also frequently discussed. A robust feed-forward strategy could be to adapt the aircraft at critical parts of the envelope from the performance-optimal configuration (low flutter damping) to a more stable flutter-optimal configuration (high damping). In principle this could be achieved by both structural and aerodynamic means. A necessary condition for an aerodynamic solution would be significant coupling of the time-mean steady background flow and the resulting motion-induced unsteady aerodynamic forces usually governing the flutter stability. While this coupling is weak in subsonic flow it occurs distinctly at transonic flow conditions, an effect to be exploited extensively within this study.

This study is largely based on the authors' previous research on fluid-mode flutter on a 2-d rectangular wing with two elastic degrees of freedom [5]. Building on the previously developed tool framework we specifically investigate the potential of steady small-scale bulges on the upper wing surface, so called Shock Control Bumps (SCB), to improve the flutter stability properties of a generic heave-pitch typical-section model in plane transonic flow (**Figure 1**). This includes explicitly the special case of buffeting at higher angles of attack, since SCBs, that were originally invented to reduce wave drag at off-design conditions [9], have been demonstrated to also have a positive effect on pure aerodynamic buffet for non-moving airfoils and wings [10, 11, 12]. Furthermore, we compare the steady SCB effect on the flutter stability and on the buffet onset to more conventional geometric changes, namely angle of attack and aileron deflection. The baseline airfoil geometry to be investigated in this study is once more the OAT15A airfoil, well-known in the shock buffet community for various numerical and experimental data sets that became recently available or are currently in production in the context of national and European research projects [13, 14, 15, 16, 17, 18, 19].

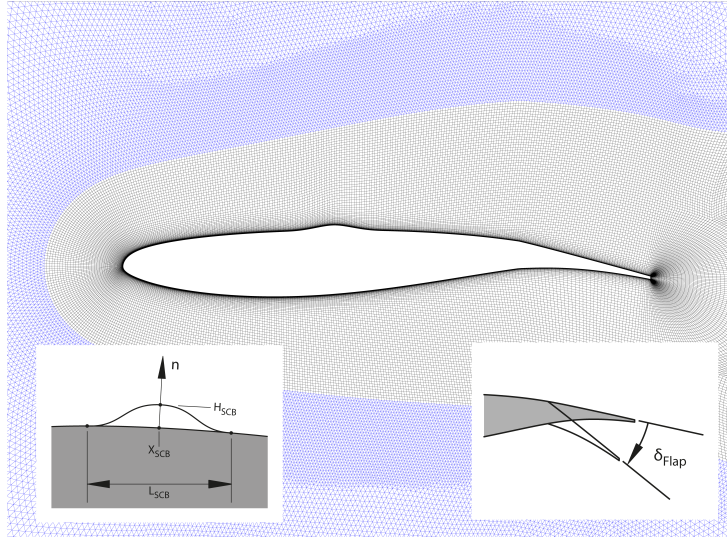


Figure 2: 2-d RANS mesh of the OAT15A airfoil with SCB and flap deformation applied
 $(X_{SCB} = 0.4c, H_{SCB} = 0.02c, L_{SCB} = 0.2c, \delta_{flap} = 5^\circ, \text{flap axis: } 75\%c)$

2 NUMERICAL MODELS AND METHODS

In this paper we aim at studying the effect of separated transonic flows at various steady operating points defined by Mach number and geometric parameters (e.g. angle of attack, SCB and flap deflection) on the flutter behavior of a simple generic 2-DOF structure with well-defined properties. Aerodynamic model and structural model exchange information via generalized (modal) coordinates and generalized aerodynamic forces (GAF). The building blocks of the modeling approach, aerodynamic model, structural model and flutter analysis are described in the following.

2.1 Aerodynamic model

We use DLR's unstructured-mesh RANS solver TAU to compute the generalized aerodynamic forces. Spatial and temporal discretization is based on experience and follows a trade between accuracy and economic considerations. **Figure 2** show the two-dimensional RANS mesh mainly used in this study. In the outer (separated) boundary layer and wake region an isotropic cell spacing of $\Delta x \approx 0.5\% c$ is realized, while the wall-tangent and wall-normal cell stretching nowhere exceeds a value of 1.2. The farfield boundary is located 100 chord lengths away from the airfoil to minimize the impact of numerical farfield reflections. The number of grid points amounts to 170 thousand. The mesh is convergent with respect to steady integral lift, drag and moment values. In addition, the reliability of the motion-induced unsteady aerodynamic forces at a reference operating point of $Ma = 0.73^\circ$ and $\alpha = 4^\circ$ (separated flow conditions) was ensured up to a reduced frequency of $\omega^* = c/V_\infty \times \omega < 1$ through a dedicated convergence study based on successively refined spatio-temporal discretization. The non-dimensional simulation time step size $\Delta t^* = \Delta t \cdot V/c$ is therefore fixed at 20% throughout this work. We employ a central Jameson-style scheme with matrix dissipation in space and an implicit BDF2 scheme in time. Mainly for reasons of robustness, we use the Spalart-Allmaras (SA) turbulence model.

To propagate the elastic mode shapes as prescribed on the airfoil surface to the surrounding volume mesh radial-basis function interpolation is used. This also includes stationary SCB and flap deformations, where the SCB shape is defined by a simple C2-smooth polynomial and the flap deformation is realized via shearing the mesh beyond the flap axis at 75% c .

Two types of grid motion are applied to the OAT15A airfoil: A rigid-body heaving motion orthogonal to the free-stream velocity vector and a rigid-body pitching motion around the quarter-chord point. The generalized aerodynamic force (GAF) response to a pitching rotation around an arbitrary rotation center along the chord is synthesized via weighted superposition of the heave response and the original quarter-chord pitch response without any noticeable error.

During an unsteady simulation run the airfoil surface is deflected with a *small-amplitude* Dirac impulse at one single time step only and the response of the GAFs (being the scalar projection of the field of aerodynamic forces on the surface onto the modal displacement field) is recorded and stored for later use in the flutter calculations. A *zero run* without any mesh motion is recorded as well and subtracted later from the Dirac-perturbed simulation results to guarantee a return of the net impulse response to exact zero for time towards infinity.

For convenience, the Reynolds number is fixed at $Re = 3 \times 10^6$ in this study including all Mach number variations.

2.2 Structural model

The structural equation of motion

$$M\ddot{q} + D\dot{q} + Kq = Q \quad (1)$$

with the generalized coordinates q and the generalized external forces Q follows the classical typical-section form:

$$\begin{bmatrix} m & S_\alpha \\ S_\alpha & I_\alpha \end{bmatrix} \begin{pmatrix} \ddot{h} \\ \ddot{\alpha} \end{pmatrix} + \begin{bmatrix} D_h & 0 \\ 0 & D_\alpha \end{bmatrix} \begin{pmatrix} \dot{h} \\ \dot{\alpha} \end{pmatrix} + \begin{bmatrix} K_h & 0 \\ 0 & K_\alpha \end{bmatrix} \begin{pmatrix} h \\ \alpha \end{pmatrix} = \begin{pmatrix} -L \\ M \end{pmatrix} \quad (2)$$

with

$$m = \mu_{ref} \rho_{ref} \pi c^2 / 4 \quad S_\alpha = x_\alpha c m \quad I_\alpha = r_\alpha^2 c^2 m \quad K_h = \omega_h^2 m \quad K_\alpha = \omega_\alpha^2 I_\alpha \\ \omega_h = \omega_{h,ref}^* V_{ref} / c \quad \omega_\alpha = \omega_{\alpha,ref}^* V_{ref} / c$$

Having a wind tunnel experiment in mind we assume that the center of gravity could ideally be placed at a pitching axis location of 40% chord. This would lead to a decoupled mass matrix. We calibrate the structural stiffness to meet a prescribed reduced frequency combination at a reference Mach number of $Ma_{ref} = 0.73$. Since we assume constant temperature ($T = 273.15$ K), the free-stream velocity, and hence, the reduced structural vacuum eigenfrequencies are a function of Mach number. At lower Mach numbers the structure becomes more high-frequency in non-dimensional terms, which is a realistic scenario. The structural configuration is defined as

$$c = 1 \text{ m} \quad \rho_{ref} = 1.225 \text{ kg m}^{-3} \quad V_{ref} = 241.84 \text{ m s}^{-1} \\ \mu_{ref} = 50 \quad x_\alpha = 0 \quad r_\alpha^2 = 0.1$$

From time to time We switch the structural eigenfrequencies of the system between the three variants 1.) "soft": $\{\omega_{h,ref}^* = 0.1, \omega_{\alpha,ref}^* = 0.2\}$, 2.) "medium": $\{\omega_{h,ref}^* = 0.2, \omega_{\alpha,ref}^* = 0.3\}$ and 3.) "stiff": $\{\omega_{h,ref}^* = 0.3, \omega_{\alpha,ref}^* = 0.4\}$.

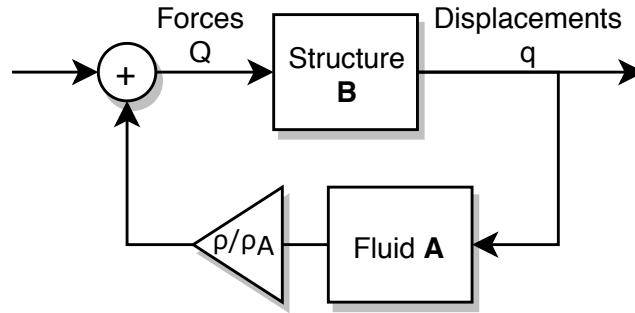


Figure 3: Aeroelastic feed-back loop with the stability parameter ρ

2.3 Flutter analysis

For the flutter stability investigations we assume the scenario of a (de-)pressurized wind tunnel. At constant Mach number, temperature and free-stream velocity we virtually increase the air density ρ (**Figure 3**). Since we keep the velocity constant while increasing density the *reduced* vacuum eigenfrequencies of the structure stay constant as well. Note that the flutter analysis is a pure post-processing step following the computationally expensive production of the aerodynamic impulse responses which are, for economic reasons, sampled at a single pair of density ρ_A and Reynolds number $Re_A = 3 \times 10^6$ only. Thus, the virtual density sweeps to study the aeroelastic system eigenvalues will match the CFD conditions at one selected point only.

As before [5], we simultaneously use three different methods to determine the aeroelastic eigenvalues of the fluid-structure coupled system as a function of fluid density. These are:

1. A direct Newton-based root search for the complex pairs (λ, x) that solve the nonlinear eigenvalue problem

$$\left[\lambda^2 M + \lambda C + K - \frac{\rho}{\rho_A} A(\lambda) \right] x = 0$$

in the frequency domain. Although being the most accurate method, the inherent weakness of this approach is that the GAF derivative matrix $A(s)$ is in principle only available along the imaginary axis. This problem is partially compensated for by a truncated Taylor expansion in the real direction. The necessary derivatives of $H(s)$ stem from the application of the Cauchy-Riemann differential equations under the reasonable assumption that the aeroelastic transfer function H is holomorphic. Nevertheless, $H(s)$ continues to be an approximation based exclusively on evaluations at $s = i\omega$ (following the classical "p-k" concept) and the method is therefore referred to as Newton-p-k (NPK).

2. The exact evaluation of the matrix-valued transfer function of the aeroelastic system in Figure 3, which reads as

$$H(s, \rho) = \left[s^2 M + sC + K - \frac{\rho}{\rho_A} A(s) \right]^{-1},$$

at $s = i\omega$ only to construct the coupled frequency response function (FRF) first. Subsequently, a rational function is fitted (RFA) to the FRF data. The RFA itself is obtained by the Vector Fitting method [20].

3. The computation of the aeroelastic impulse response function in the time domain with subsequent identification of the complex eigenvalues in the discrete time signals. The

lossless construction of the fluid-structure coupled impulse response follows a novel successive convolution algorithm (SCM, [5]). Once the coupled impulse response sequence is available we employ the Ibrahim time-domain technique [21] (which is also at the core of the so called Dynamic Mode Decomposition) to recover the eigenvalue and eigenvector information from the complex-exponential impulse response signals.

3 RESULTS

3.1 Transonic buffet and pre-buffet on the clean airfoil

Before we turn to the influence of geometric modifications, we will first give an overview of the buffet behavior of the original clean geometry of the OAT15A profile. For this purpose, unsteady simulations were carried out for different combinations of Mach number and angle of attack on the *non-moving* mesh. Each unsteady simulation re-starts from a steady-state solution, which could be easily generated in almost all cases by running the CFD solver in steady-state mode. **Figure 4** shows in each case the lift coefficient c_L over time. For convenience, all time signals were scaled and plotted at the respective Ma - α combination. The black dot marks $t = 0$ and an offset of $c_L = 1$. Temporally stable responses of the flow are colored in blue, unstable ones in red. Clearly visible is an inclined, elongated region of instability. Frequency and amplification rate at the steady fixed point as well as final amplitude of the final limit-cycle oscillation vary. Note that in contrast to frequency and damping close to the steady fixed point (i.e. for small amplitudes), the grid convergence in time and space cannot be guaranteed for the limit cycle amplitudes. However, the purpose of this overview is only the identification of the buffet onset and this should be reliable. Self-excited shock buffeting oscillations can be observed for the OAT15A airfoil and employing the SA turbulence model only at high angles of attack above $\alpha > 4.5^\circ$ and Mach numbers $Ma < 0.72$. Simulations employing other turbulence models (not shown here) lead to slightly different buffet onsets and in tendency larger instability regions. Qualitatively, however, no major differences occur.

We continue an initial characterization of the dynamic flow behavior with a look at the motion-induced unsteady aerodynamic forces in the stable region outside the buffet onset. At two selected Mach numbers $Ma = 0.68$ and 0.73 we vary the angle of attack and construct the complex-valued frequency response of the derivative of the dynamic lift with respect to a small pitch motion around the quarter-chord point $c_{L,\alpha}$. For lower angles of attack and attached flow conditions, a typical curve for $c_{L,\alpha}$ is obtained in the frequency domain (magnitude plotted here), which qualitatively resembles the well-known Theodorsen function (**Figure 5**). If the angle of attack is increased, a distinct resonance peak appears in the aerodynamic transfer function. The position and height of the resonance peak maximum vary with α and Ma . When the buffet onset is reached, the resonance peak approaches infinity. The resonance peak can be viewed as the footprint of a complex pole (eigenvalue) with negative real part in the transfer function of an equivalent linear time-invariant (LTI) system valid for small-perturbation inputs at a specific operating point [2].

Figure 6 is used to correlate steady-state flow field properties and the dominating aerodynamic eigenfrequency. In the upper part, the steady-state lift coefficient is depicted versus the angle of attack for the two Mach numbers $Ma = 0.68$ and 0.73 . For the higher one (in blue), all steady solutions are stable. For the lower one (red), self-excited buffet oscillations occur beyond the lift maximum in a range of $5.4 < \alpha < 8.0$ (recall Figure 4). Therefore, minimum and maximum values during the buffet LCO (peak-to-peak) are additionally shown here. In the lower part, the

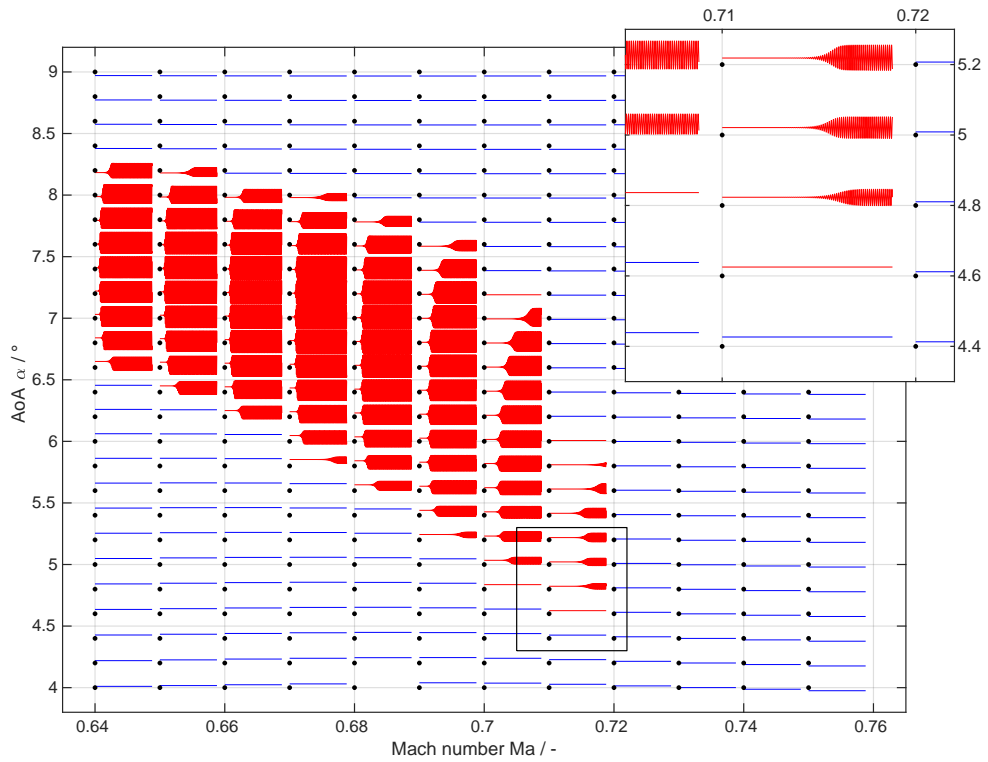


Figure 4: Overview of the unstable shock buffet region in the Ma- α plane.

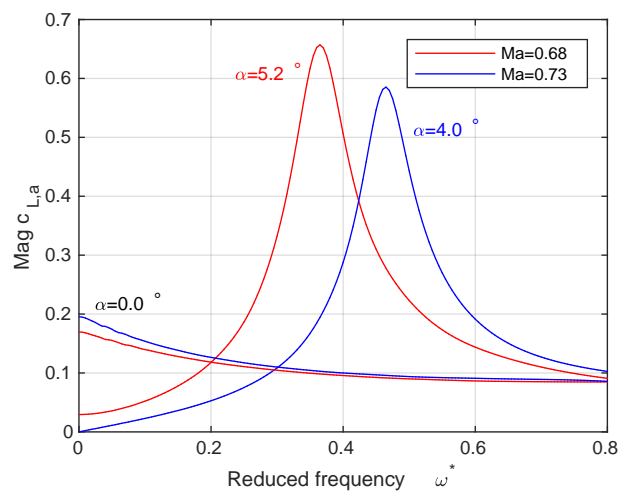


Figure 5: Frequency response of the $c_{L,\alpha}$ magnitude for attached flow conditions at low angles of attack in comparison to separated flow conditions exhibiting pronounced aerodynamic resonance peaks

position of the shock on the suction side as identified from the location of the jump in surface pressure x_s is also depicted. Initially, the shock moves downstream towards the trailing edge as the angle of attack increases. With increasing shock strength, the thickness of the downstream boundary layer grows over-proportionally and the shock begins to move upstream. This reversal of the shock motion (sometimes termed *inverse shock motion*) can be regarded as a reliable criterion for shock-induced boundary layer separation. Furthermore, the center positions and lengths of three different SCBs are plotted here, that will be investigated later in section 3.3.2. In the lower part of Figure 6 the location ω_{peak}^* and height of the aerodynamic resonance maximum $c_{L,\alpha \text{ peak}}$ is depicted. For the stable flows at $\text{Ma} = 0.73$, the frequency maximum first occurs above $\alpha > 2^\circ$ and reaches a maximum at $\alpha \approx 4^\circ$. Here the damping of the natural oscillation becomes minimal. With increasing angle of attack and increasing distance from the buffet onset, the damping increases again and the resonance peak becomes lower. The peak frequency increases continuously with the angle of attack. The increase accelerates for higher angles. For Mach 0.68, a similar curve occurs below the buffet onset, but shifted upwards by about 2 degrees. However, the height of the resonance peak then approaches infinity. The pole of the equivalent LTI system is now located directly on the imaginary axis of the Laplace domain. Inside the buffet region, the determination of the dominant eigenvalue (now with positive real part) is no longer feasible via simple input-output identification. As a substitute, the reduced frequency of the buffet limit cycle solution ω_{buffet}^* is shown here, as it can be easily extracted from the time signals (see 4). Above the buffet region the frequency maximum in $c_{L,\alpha}$ can be identified again and shows a comparable steep increase as at $\text{Ma} = 0.73$. To the authors' knowledge, there is still no known consistent theoretical model that provides a satisfactory explanation for this behavior, which is observable in both numerical simulation (e.g. [16]) and wind tunnel experiments.

3.2 SCB Design

In this study, we examine how SCBs affect the (fluid-mode) flutter behavior. The first question is how these bumps should be dimensioned. We initially follow a reduced, purely aerodynamic approach (as in [12]) and postpone the test of the actual effectiveness of the design with respect to flutter until later. Starting from Figure 4, we decide to focus on two working points at $\text{Ma} = 0.68$. The goal is to completely eliminate the self-excited aerodynamic buffet oscillations by introducing a stationary SCB on the suction side of the airfoil. For this purpose, we investigate $\alpha = 5.7^\circ$ near the lower buffet onset and $\alpha = 6.7^\circ$ in the center of the buffet region. Feasible designs can be easily found for both cases by trial and error. **Figure 7** shows the simulation results again in the form of a lift versus time plot (analogous to Figure 4) for different SCB heights H_{SCB} and center positions X_{SCB} , keeping the bump length constant at $L_{SCB} = 20\% c$ in each case. Clearly visible, the unstable flow can be stabilized. If one also wants to approximately keep the steady lift of the airfoil with SCB constant compared to the airfoil without SCB, a line of possible bump heights results. Here, for robustness reasons, an SCB height of $0.5\% c$ was chosen (star symbol). At $\alpha = 5.7^\circ$ this strategy results in an optimal center position of $X_{SCB} = 34.8\% c$ (SCB 1) and at $\alpha = 6.7^\circ$ of $X_{SCB} = 23.3\% c$ (SCB 2). Note that these optimal positions correlate well with the steady shock location x_s as plotted in Figure 6. Apart from these two more robust designs it is worth noting that remarkably small bump heights in the order of $0.1\% c$ may be enough to eliminate severe buffet completely, at least from a narrow local point of view.

Figure 8 shows on the left the off-design behavior of both SCB designs at $\text{Ma} = 0.68$ still being constant. Both designs obviously develop some effectiveness outside their design points (star

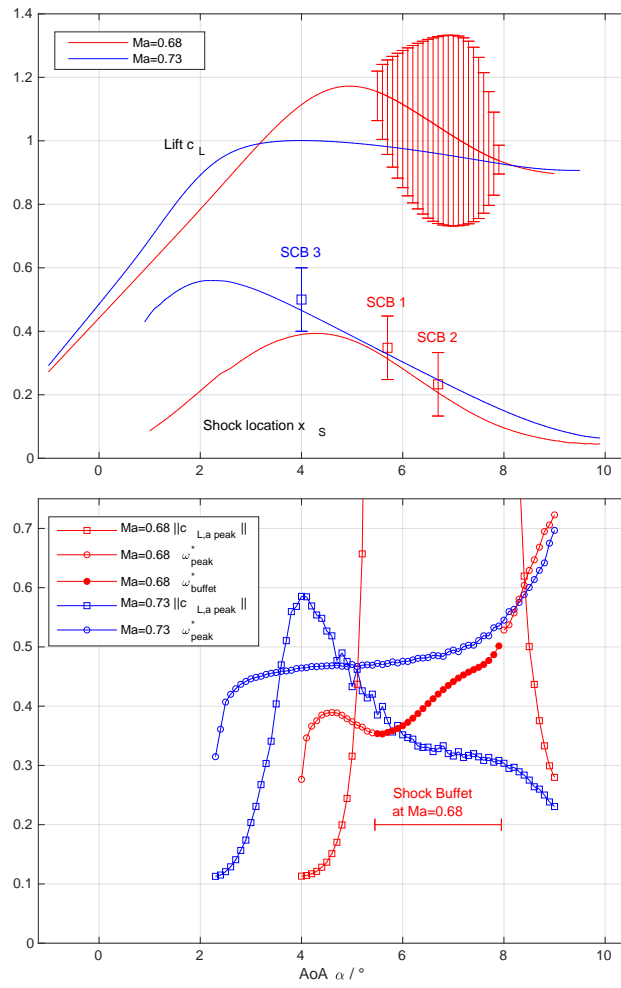


Figure 6: Steady and unsteady flow characteristics at $Ma = 0.68$ and $Ma = 0.73$

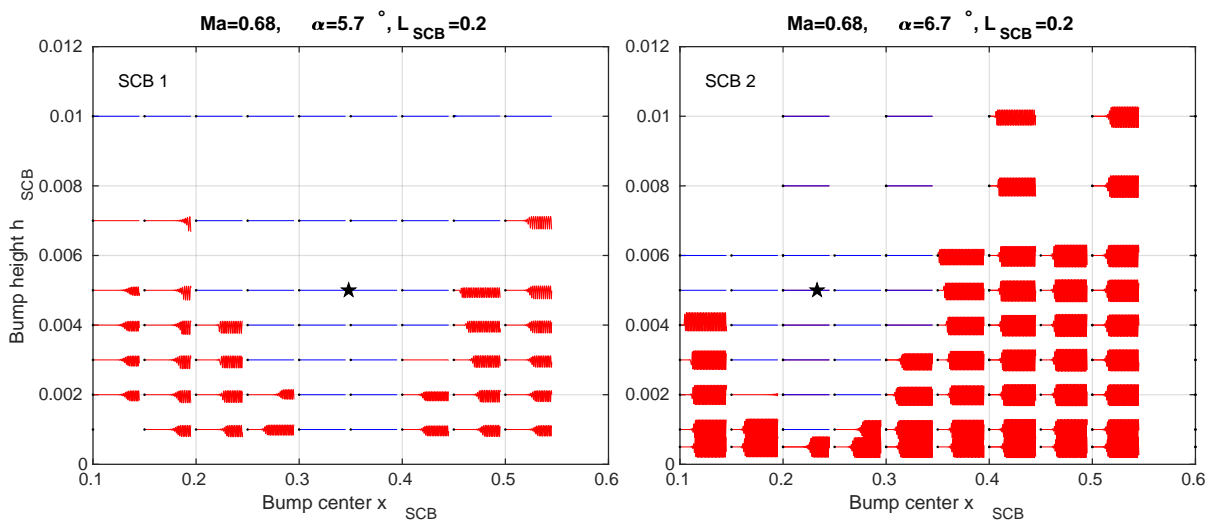


Figure 7: Design of SCBs by trial-and-error variation of bump center X_{SCB} bump height H_{SCB} at constant bump length $L_{SCB} = 20\% c$

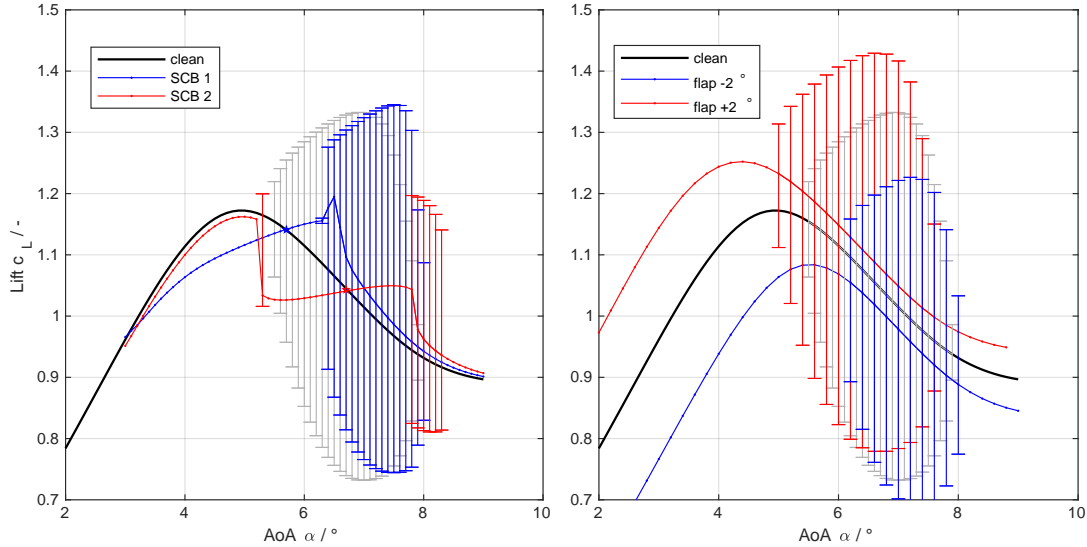


Figure 8: Aerodynamic off-design behavior of SCB 1 and SCB 2 (left) in comparison to conventional flap deflections (right)

symbols). However, the idea of keeping the lift of the airfoil constant by local optimization turns out not to be very viable. Beyond the design points, the lift polar is strongly changed. Discontinuities seem to be formed. At least at SCB 2, one can assume that hysteresis occurs here due to solution bifurcation. On the other hand, SCB 2 is very effective in terms of buffet suppression, but is probably a bit too far upstream. SCB 1 shifts the buffet onset significantly, but changes the polars strongly near the lift maximum.

At this point, the effect of SCBs is compared to a more conventional flap deflection. The right of **Figure 8** shows the buffet behavior with a trailing edge flap deflection of $\delta \pm 2^\circ$. The effect is completely different from that of the SCBs. Essentially, the lift polar including the buffet region is merely shifted. Nevertheless, it can be stated that a de-cambering of the profile by negative flap deflection could be a suitable strategy to shift the buffet onset or to reduce the amplitude of the buffet oscillations.

3.3 Flutter behavior

We now proceed to the actual flutter analyses in the vicinity of the buffet onset. For this purpose we compare the behavior of the soft, medium and stiff generic structures as detailed in Section 2.2. We virtually increase the wind tunnel density and observe the eigenvalues of the aeroelastic system as they are identified simultaneously by each of the three different computational methods described in Section 2.3. Zero crossings of a real part define a flutter point. The stability limit curves shown in the following vary on the one hand with the structural parameters of the underlying 2-DOF system and on the other hand with the aerodynamic operating points. The stability curves are partly the envelope over several flutter mechanisms including static divergence due to the fact that the pitch axis of our systems is located relatively far back at $40\%c$. To ensure comparability for different Mach numbers, we plot the critical flutter density ρ_f in terms of the respective critical dynamic pressure $q_f = \rho_f(aMa)^2/2$ with a being the speed of sound.

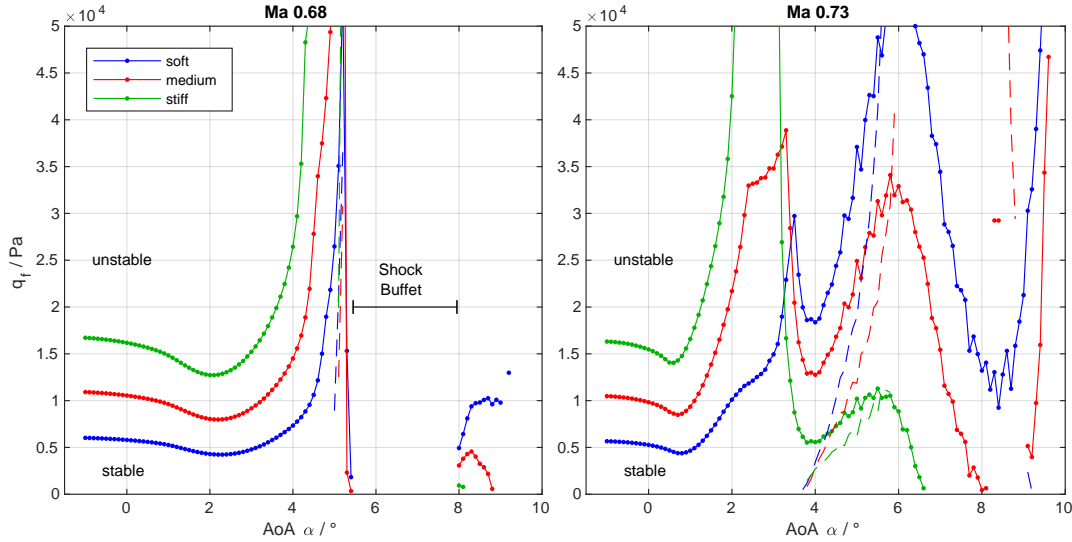


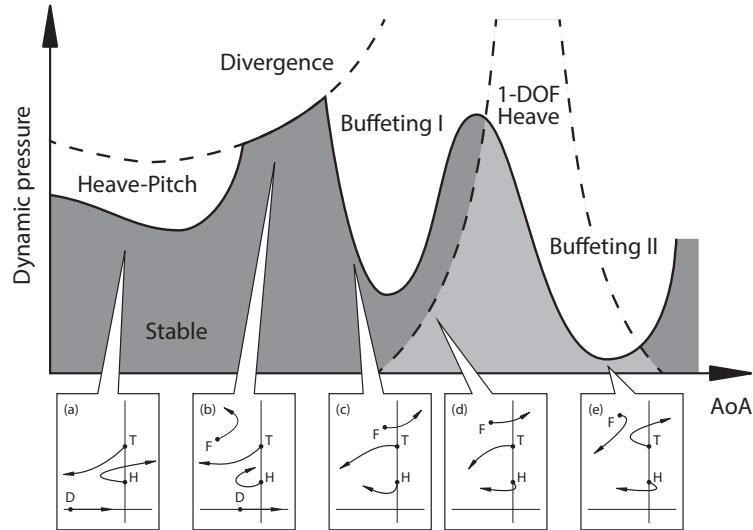
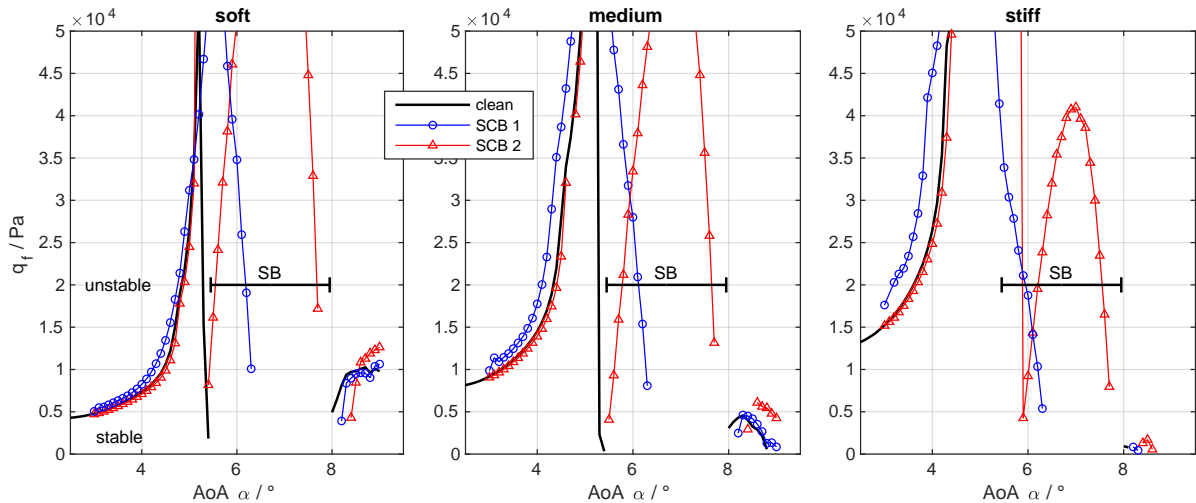
Figure 9: Flutter and buffeting behavior of the clean airfoil at two different Mach numbers

3.3.1 Clean airfoil

In the beginning we consider the unmodified profile as a reference. **Figure 9** shows the critical values for the dynamic pressure q_f versus α at $Ma = 0.68$ and $Ma = 0.73$. When we approach to the buffet onset head-on at $Ma = 0.68$ the flutter behavior is rather conventional at first. Classic bending-torsion flutter occurs. Only from $\alpha > 4^\circ$ (cf. Figure 6) a complex fluid mode can be detected in the aerodynamic frequency response at all (cf. 6). Interestingly, the flutter stability then increases abruptly instead of decreasing continuously as one could also have assumed. Classical flutter and fluid-mode flutter are clearly separated from each other by an apparent wall of stability. The expected reduction of the effective buffet onset compared to the purely aerodynamically identified value by adding structural elasticity is in the order of $0.1^\circ - 0.2^\circ$ deg and thus turns out to be marginal.

The situation is different at $Ma=0.73$. At this Mach number, as mentioned, no self-excited shock buffet occurs at all from a purely aerodynamic point of view. Nevertheless, fluid-mode flutter occurs when structural elasticity is added. The results shown in Figure 9 (right) agree quite well with the behavior already observed in [5], but are presented here in much higher resolution. At present it is not clear why the flutter curves for higher angles of attack appear much noisier than for lower angles. Problems may be due to deficiencies in tempo-spatial discretization due to the under-resolution of the massively separated flow. For clarity, the principle behavior along the angle of attack at $Ma = 0.73$ is reproduced schematically in **Figure 10**. At low angles of attack we see classical flutter due to the coupling of heave (H) and torsion (T). This is succeeded as a critical mechanism by the static divergence (D), if the torsional stiffness is low enough. If this is not the case, a similar wall of stability as already observed at $Ma = 0.68$ arises. After that, a stability drop (Buffeting I) occurs under the participation of the fluid mode (F). The closer the structural torsional natural frequency is to the aerodynamic resonance frequency, the more severe appears the drop. This can be followed by a region of renewed stabilization, which is then followed by an even deeper reduction (Buffeting II) where finally the torsional motion experiences 1-DOF flutter from density zero. The latter is associated with a qualitative switching of the critical flutter branch. While in Buffeting I the original fluid mode becomes unstable, in Buffeting II the torsional branch becomes unstable.

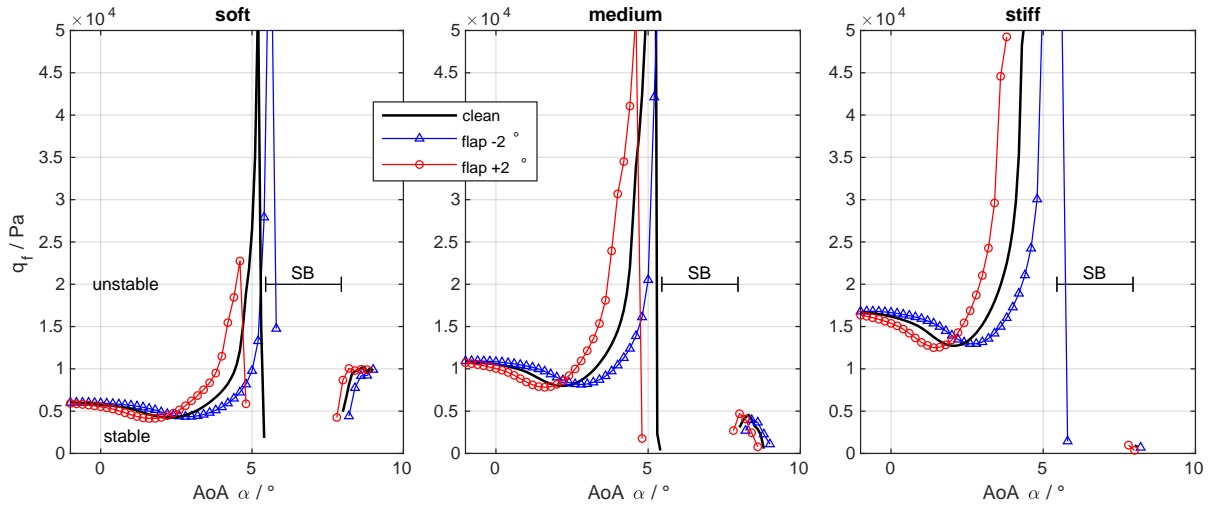
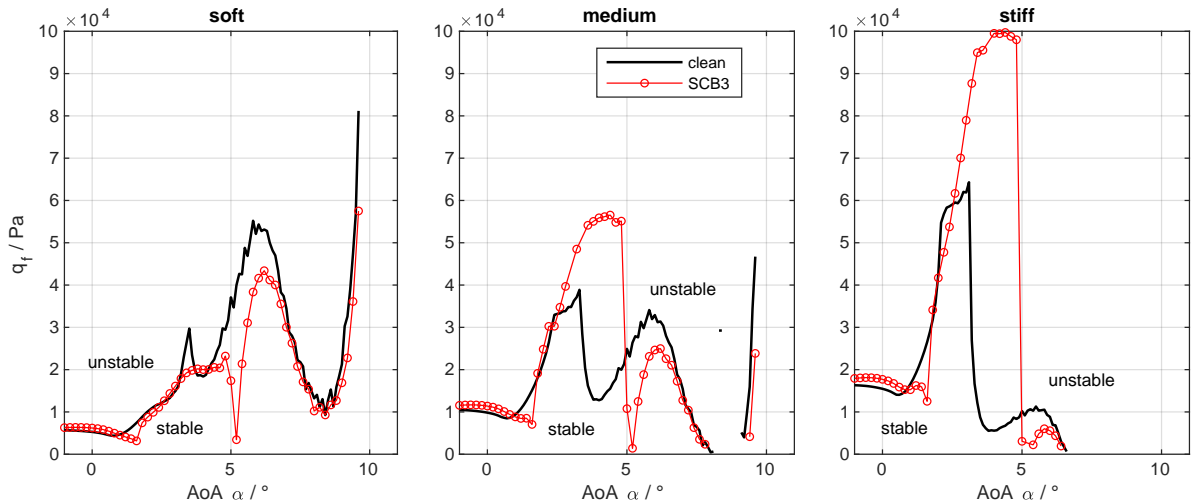
In the generic example specifically discussed in this study, an additional complication arises.


 Figure 10: Schematic view of the flutter mechanisms at $Ma = 0.73$

 Figure 11: SCB effect on the flutter behavior at $Ma = 0.68$

Since it was deliberately decided to structurally decouple the heave and torsion degrees of freedom (cf. Section 2.2), 1-DOF flutter of the low-frequency heave DOF occurs as soon as the steady $\partial c_L / \partial \alpha$ becomes negative (stall flutter). This means that in a certain angle of attack range the heave DOF is immediately unstable beginning from density zero and stabilizes only later when a pitch component is introduced by the aerodynamic coupling. These reversed instability regions appear as dashed lines in the flutter plots but are sometimes hardly detected at all due to algorithmic difficulties. For the moment they can be seen as artefacts that are in principle avoidable by adding some off-diagonal static moment to the structural mass matrix.

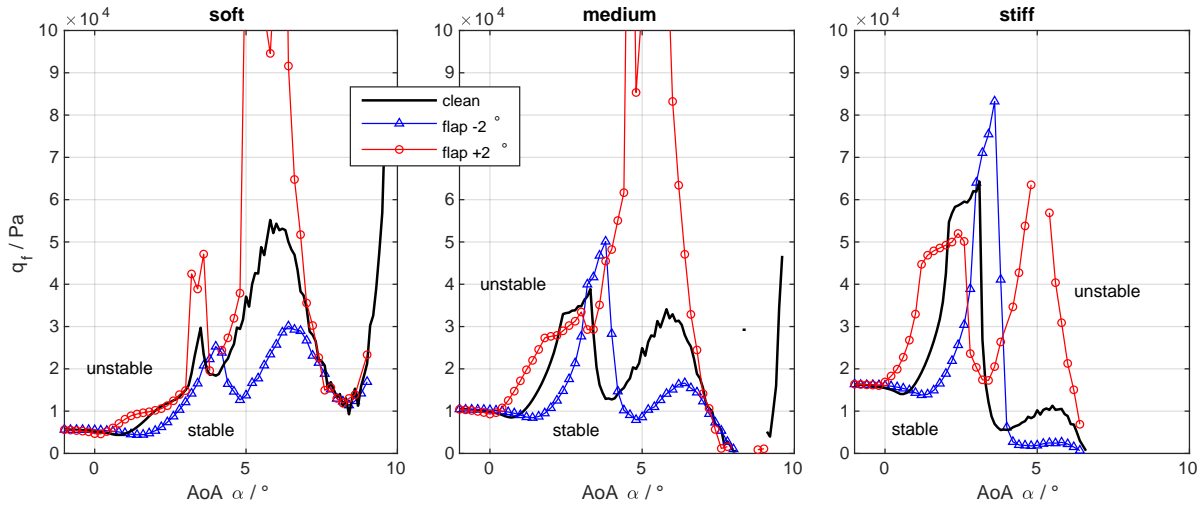
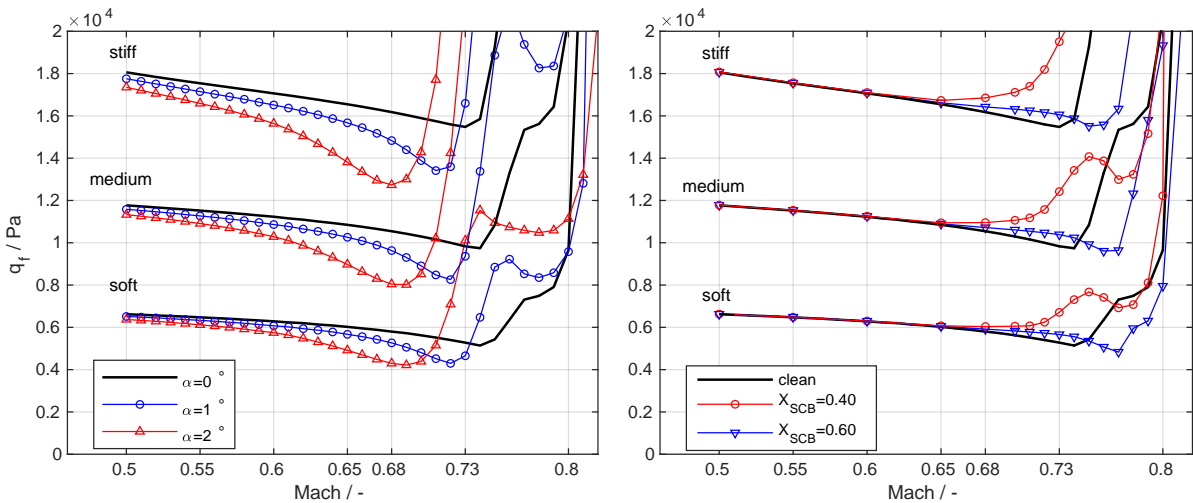
3.3.2 SCB and flap effects

In the following, we will investigate how geometric modifications in the form of SCBs and flap deflections affect the flutter and buffeting behavior and, in particular, whether the findings from a purely aerodynamic analysis can also be transferred to the flutter behavior without further ado or whether there may even be opposite effects.

Figure 12: Flap effect on the flutter behavior at $Ma = 0.68$ Figure 13: SCB effect on the flutter behavior at $Ma = 0.73$

We start again with $Ma = 0.68$ and look at the influence of SCB 1 and SCB 2 on the flutter behavior compared to the clean profile. **Figure 11** shows the stability curves for our three structural configurations side by side. SCB 1 increases the effective buffet onset by about 1° . SCB 2 becomes effective at higher angles of attack and effectively prevents fluid-mode flutter in the former buffet region. At the limits of the effective range, however, the stability drops noticeably. In the low angle of attack range, the SCBs are practically ineffective. This behavior is largely identical to what would be expected from pure aerodynamic analysis (cf. Figure 8). The same holds true for the less spectacular effect of the trailing edge flap on flutter, which for completeness is shown in **Figure 12**. Again, the flutter behavior is analogous to the aerodynamic buffet behavior: A flap deflection essentially causes a simple shift and partial compression of the flutter curve along the angle of attack axis.

At Mach 0.73, SCB 1 and SCB 2 were also initially used, but they proved to be hardly effective in the suppression of the stability drop at $\alpha \approx 4^\circ$, which could be regarded as an *elastic buffet onset* and which particularly affects the stiff configuration due to the close frequency neighborhood of the torsion mode to the fluid mode. It was found that a downstream shift of the bump to $X_{SCB} = 50\% c$ at a length of $L_{SCB} = 20\% c$ (SCB 3) was necessary here. This aligns again with the basic idea that SCBs only come to effect if they are placed near the shock (cf. Figure

Figure 14: Flap effect on the flutter behavior at $Ma = 0.73$ Figure 15: Flutter behavior at low constant angle of attack of the clean airfoil (left) in comparison to SCB-modified airfoils at $\alpha = 0^\circ$ (right)

6). In this case, the flutter behavior shown in **Figure 13** can be observed and a shift of the elastic buffet onset of $\approx 1.5^\circ$ is feasible. It appears to be more difficult here to develop sufficient effect with a bump length of 20%. With longer bumps one could probably achieve greater effects although the technical feasibility may be questionable. Again for the sake of completeness, we show in **Figure 14** the effect of flap deflections at $Ma = 0.73$. In the lower angle of attack range, again a simple shift of the effective angle of attack range can be observed.

A final interesting aspect arises if the use of SCBs is not considered in the conventional sense, i.e. for buffet control, but instead SCBs are applied specifically in attached flow conditions in order to possibly improve the classical flutter behavior in the sense of a semi-active flutter suppression strategy. **Figure 15** shows the curves of the critical dynamic pressure q_f this time versus Mach number at constant angle of attack. The well-known transonic dip shapes can be observed. For reference, the effect of the angle of attack is being considered first on the left. An increased angle of attack has a globally lowering effect on the flutter boundary. In comparison, two different SCBs with a standard height a 0.5% c and length of 20% c are placed on the upper airfoil side, once at $X_{SCB} = 40\% c$ and once at $60\% c$. In the example shown here, a significant improvement of the classical flutter behavior in the range of the transonic dip was

achieved with the bump center at 40%. However, if the SCB was placed too far downstream, the global flutter behavior deteriorated in comparison with the clean profile. The cause of the (de-)stabilizing effect is probably to be found in the introduction of additional re-compression shocks in previously shock-free flow regions and is currently being investigated.

4 CONCLUSIONS

In this study, we have investigated the effects of geometric modifications, in particular so-called shock control bumps, on the transonic buffeting and flutter behavior of a classical typical-section two-degree-of-freedom model. Special attention was paid to the possibility of so-called fluid-mode flutter, i.e., the unfavorable coupling of fluid modes and structural modes in separated flow conditions. We were able to show exemplarily that SCBs, compared to conventional trailing edge flap deflections, are suited for influencing the aerodynamic and aeroelastic behavior at edge-of-envelope flight conditions in the desired direction. The results shown here also indicate that a purely aerodynamically driven SCB design approach may be sufficient in the first place, since no contradicting aeroelastic effects could be detected. Initial results indicate that SCBs can also be used in attached flow in the transonic dip region to improve the classical flutter behavior. Aspects of technical feasibility and integration into overall flight control were not considered.

SCBs and flap deflections were dealt with separately in this work. However, it could be useful to combine the two, on the one hand to place compression shocks specifically in the vicinity of SCBs and, on the other hand, to address the problem of trim, which was omitted here. The determination of the flutter behavior in complex flows possibly involving fluid modes was conducted here using experimental flutter analysis methods that rely on input-output identification of the applied RANS solver but are far from having the robustness necessary for routine use in the design and optimization processes. Future time-linearized methods aiming at a global eigenvalue analysis of the Jacobian matrix of the fluid-structure coupled system may yield further improvements in this respect.

ACKNOWLEDGEMENTS

Parts of the research leading to this work have received funding from the the German Federal Ministry of Economic Affairs and Climate Action (BMWK) in the framework of the Federal Aeronautical Research Program (LuFo) V-3 within the project Move-IntegR (FKZ: 20W1729C).

5 REFERENCES

- [1] Abbas-Bayoumi, A. and Becker, K. (2011). An industrial view on numerical simulation for aircraft aerodynamic design. *Journal of Mathematics in Industry*, 1(1), 10. doi: 10.1186/2190-5983-1-10.
- [2] Nitzsche, J. (2009). A numerical study on aerodynamic resonance in transonic separated flow. In *Proc. of the 13th International Forum on Aeroelasticity and Structural Dynamics (IFASD)*, Seattle, WA, USA, 22-24 June 2009.
- [3] Iovnovich, M. and Raveh, D. E. (2011). Transonic unsteady aerodynamics in the vicinity of shock-buffet instability. In *Proc. of the 14th International Forum on Aeroelasticity and Structural Dynamics (IFASD)*, Paris, France, 27-30 June 2011.

- [4] Giannelis, N. F., Vio, G. A., and Levinski, O. (2017). A review of recent developments in the understanding of transonic shock buffet. *Progress in Aerospace Sciences*, 92, 39–84. doi:10.1016/j.paerosci.2017.05.004.
- [5] Nitzsche, J., Ringel, L. M., Kaiser, C., et al. (2019). Fluid-mode flutter in plane transonic flows. Paper IFASD-2019-006. In *Proc. of the 18th International Forum on Aeroelasticity and Structural Dynamics (IFASD), Savannah, GA, USA, 9-13 June 2019*.
- [6] Gao, C., Zhang, W., and Ye, Z. (2018). Reduction of transonic buffet onset for a wing with activated elasticity. *Aerospace Science and Technology*, 77, 670–676. doi:10.1016/j.ast.2018.03.047.
- [7] Gao, C. and Zhang, W. (2020). Transonic aeroelasticity: A new perspective from the fluid mode. *Progress in Aerospace Sciences*, 113, 100596. ISSN 0376-0421. doi:https://doi.org/10.1016/j.paerosci.2019.100596.
- [8] Houtman, J. and Timme, S. *Towards Global Stability Analysis of Flexible Aircraft in Edge-of-the-Envelope Flow*. doi:10.2514/6.2021-0610.
- [9] Künnecke, S. C., Vasista, S., Riemenschneider, J., et al. (2021). Review of adaptive shock control systems. *Applied Sciences*, 11(2). ISSN 2076-3417. doi:10.3390/app11020817.
- [10] Mayer, R., Lutz, T., and Krämer, E. (2018). Numerical study on the ability of shock control bumps for buffet control. *AIAA Journal*, 56(5), 1978–1987. doi:10.2514/1.J056737.
- [11] Mayer, R., Lutz, T., Krämer, E., et al. (2019). Control of transonic buffet by shock control bumps on wing-body configuration. *Journal of Aircraft*, 56(2), 556–568. doi:10.2514/1.C034969.
- [12] Geoghegan, J. A., Giannelis, N. F., and Vio, G. A. (2020). A numerical investigation of the geometric parametrisation of shock control bumps for transonic shock oscillation control. *Fluids*, 5(2), 46. doi:10.3390/fluids5020046.
- [13] Deck, S. (2005). Numerical simulation of transonic buffet over a supercritical airfoil. *AIAA Journal*, 43, 1556–1566. doi:10.2514/1.9885.
- [14] Jacquin, L., Molton, P., Deck, S., et al. (2009). Experimental study of shock oscillation over a transonic supercritical profile. *AIAA Journal*, 47, 1985–1994. doi:10.2514/1.30190.
- [15] Illi, S., Lutz, T., and Krämer, E. (2012). On the capability of unsteady RANS to predict transonic buffet. In *Third Symposium "Simulation of Wing and Nacelle Stall", Braunschweig, Germany, 21-22 June*.
- [16] Giannelis, N. F., Levinski, O., and Vio, G. A. (2018). Influence of Mach number and angle of attack on the two-dimensional transonic buffet phenomenon. *Aerospace Science and Technology*, 78, 89 – 101. doi:10.1016/j.ast.2018.03.045.
- [17] Zimmermann, D.-M., Mayer, R., Lutz, T., et al. (2018). Impact of Model Parameters of SALSA Turbulence Model on Transonic Buffet Prediction. *AIAA Journal*, 56, 874–877. doi:10.2514/1.J056193.

- [18] Accorinti, A., Baur, T., Scharnowski, S., et al. (2021). Measurements of deformation, schlieren and forces on an OAT15A airfoil at pre-buffet and buffet conditions. *IOP Conference Series: Materials Science and Engineering*, 1024(1), 012052. doi:10.1088/1757-899x/1024/1/012052.
- [19] D'Aguanno, A., Schrijer, F. F. J., and van Oudheusden, B. W. (2021). Experimental investigation of the transonic buffet cycle on a supercritical airfoil. *Experiments in Fluids*, 62(10), 214. ISSN 1432-1114. doi:10.1007/s00348-021-03319-z.
- [20] Gustavsen, B. and Semlyen, A. (1999). Rational approximation of frequency domain responses by vector fitting. *IEEE Transactions on Power Delivery*, 14(3), 1052–1061. doi:10.1109/61.772353.
- [21] Ibrahim, S. and Mikulcik, E. (1977). A method for the direct identification of vibration parameter from the free response. *Shock and Vibration Bulletin*, 47, 183–198.

COPYRIGHT STATEMENT

The authors confirm that they, and/or their company or organization, hold copyright on all of the original material included in this paper. The authors also confirm that they have obtained permission, from the copyright holder of any third party material included in this paper, to publish it as part of their paper. The authors confirm that they give permission, or have obtained permission from the copyright holder of this paper, for the publication and distribution of this paper as part of the IFASD-2022 proceedings or as individual off-prints from the proceedings.